





# **Accepted Manuscript**



This article can be cited before page numbers have been issued, to do this please use: N. Sparks, A. Dorris, S. Vijayan, I. Chandrasiri, F. Zia, A. Flynt, N. I. Hammer and D. Watkins, *Mol. Syst. Des. Eng.*, 2022, DOI: 10.1039/D2ME00014H.



This is an Accepted Manuscript, which has been through the Royal Society of Chemistry peer review process and has been accepted for publication.

Accepted Manuscripts are published online shortly after acceptance, before technical editing, formatting and proof reading. Using this free service, authors can make their results available to the community, in citable form, before we publish the edited article. We will replace this Accepted Manuscript with the edited and formatted Advance Article as soon as it is available.

You can find more information about Accepted Manuscripts in the <u>Information for Authors</u>.

Please note that technical editing may introduce minor changes to the text and/or graphics, which may alter content. The journal's standard <u>Terms & Conditions</u> and the <u>Ethical guidelines</u> still apply. In no event shall the Royal Society of Chemistry be held responsible for any errors or omissions in this Accepted Manuscript or any consequences arising from the use of any information it contains.



The ability to modulate the optical properties of a fluorophore by altering its microenvironment offers transformative advances in the field of bioimaging. This work aimed to study the effects that encapsulation has on the optical properties of a functionalizable donor-acceptor-donor (DAD) NIR-emissive fluorophore. Parallel studies in which a NIR-emissive fluorophore was uptaken into a dendritic copolymer and developed into an amphiphile provided two nanoaggregate systems exhibiting uniquely different optical properties in aqueous media. *In vitro* experiments supported the applicability of the nanoaggregates as potential imaging agents. This work lays the foundation for further probing polymer-fluorophore interactions as essential "bottom-up" tactics for NIR bioimaging applications.

View Article Online DOI: 10.1039/D2ME00014H

# **ARTICLE**

# Effects of Nanoaggregation on Isoindigo-based Fluorophores for Near-infrared Bioimaging Applications

Received 00th January 20xx, Accepted 00th January 20xx

DOI: 10.1039/x0xx00000x

Nicholas E. Sparks,<sup>‡ a</sup> Austin Dorris,<sup>‡ a</sup> Sajith M. Vijayan,<sup>a</sup> Indika Chandrasiri,<sup>a</sup> Mohammad Farid Zia,<sup>b</sup> Alex Flynt,<sup>b</sup> Nathan I. Hammer,<sup>\* a</sup> and Davita L. Watkins<sup>\* a</sup>

In this work, we have taken a D-A-D fluorophore (II-EDOT-TPA) and encapsulated it using a linear dendritic block copolymer (LDBC). In parallel, a polyethylene glycol derivative (PEG-II-EDOT-TPA) was synthesized. The self-assembly and colloidal properties of both nanoaggregates were comparatively assessed. Photophysical and morphological characterization of the LDBC encapsulated II-EDOT-TPA and PEG-II-EDOT-TPA nanoaggregates was performed, which showed the photophysical and morphological properties differed greatly when comparing the two. Both nanoaggregate types were incubated with HEK-293 cells in order to measure cell viability and perform confocal fluorescence microscopy. Minimal cytotoxicity values (<20%) were seen with the two nanoaggregate forms, while both types of nanoaggregates were found to accumulate into the lysosomes of the HEK-293 cells. This work provides fascinating insights into NIR fluorophore design and methods to effectively alter the photophysical and morphological properties of the nanoaggregates for bio-imaging purposes.

#### Introduction

Published on 27 April 2022. Downloaded on 4/27/2022 11:34:58 PM

As the use of fluorescence bioimaging increases in popularity, we aim to design novel highly emissive near-infrared (NIR) organic fluorophores to perform in vivo fluorescence bioimaging. To date, NIR organic fluorophores have faced both photophysical and biocompatibility challenges, to which the application of NIR organic fluorophores for use in practical applications faces multiple barriers. The emissive properties of conventional organic fluorophores are often affected by aggregation-caused quenching (ACQ), which occurs upon an increase in the concentration of the fluorophores in solution or in the solid-state. The emissive properties of the fluorophores are either diminished or completely quenched in this aggregated state relative to dilute solutions of the fluorophores.<sup>1, 2</sup> The quenching is due to intermolecular  $\pi$ - $\pi$ stacking between the adjacent conjugated systems and aromatic rings of the fluorophores, which upon excitation and subsequent relaxation, allows for non-radiative decay to the ground state.

In contrast, one phenomenon that takes advantage of aggregated fluorophores is aggregation-induced emission (AIE).<sup>3, 4</sup> Fluorophores that possess this ability are non- or weakly-emissive in dilute solution but experience a noticeable increase in emissive properties upon aggregation. The term AIE

was first reported by Tang et. al., where differences in the emissive properties for 1-methyl-1,2,3,4,5,-pentaphenylsilole when changing from dilute solution to an aggregated form of the compound were reported.<sup>5,6</sup> Since then, the exploitation of AIE has led to an

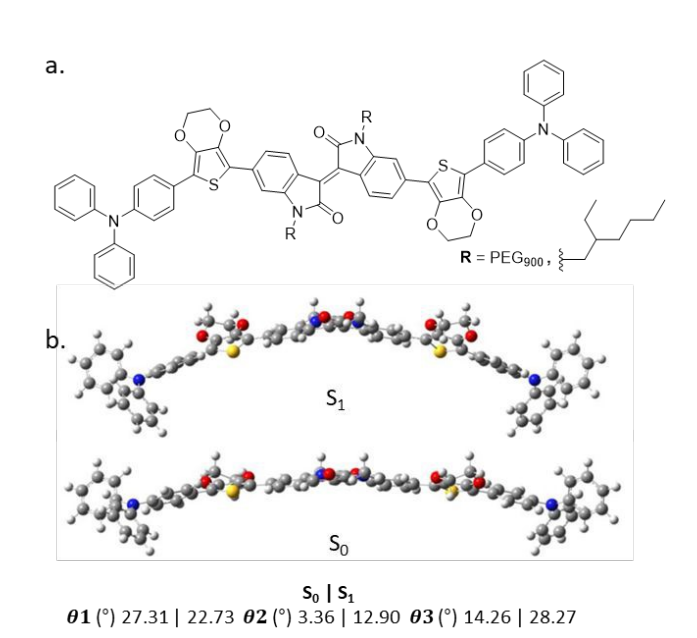


**Figure 1.** Structures of **II-EDOT-TPA** (a) and optimized ground and excited state geometries of **II-EDOT-TPA** in the gas phase with the use of TD-OT- $\omega$ B97XD/6-311G(d,p)//B3LYP/6-311G(d,p) level of theory. <sup>7</sup>

increase in research focused on materials that can exploit this phenomenon for practical applications.

Electronic Supplementary Information (ESI) available: [details of any supplementary information available should be included here]. See DOI: 10.1039/x0xx00000x

<sup>&</sup>lt;sup>a.</sup> Department of Chemistry and Biochemistry, University of Mississippi, University, MS 38677, United States

b. Department of Biological Sciences, The University of Southern Mississippi, Hattiesburg, MS, 39406, United States.

<sup>‡</sup> Equal intellectual contribution

Published on 27 April 2022. Downloaded on 4/27/2022 11:34:58 PM

ARTICLE Journal Name

As interest in AIE active materials increases, so do our understanding of the structural and photophysical properties associated with them.<sup>8, 9</sup> A general structural characteristic of AIE fluorophores is the presence of an aromatic substituent that rotates freely in dilute solution. These intramolecular rotations are inhibited when the fluorophores are aggregated, which is referred to as a restriction of intramolecular rotations (RIR).<sup>10</sup> In addition to the RIR mechanism, the restriction of intramolecular vibrational (RIV) motions also contributes to the AIE phenomenon. The combined RIR and RIV mechanisms are known collectively as the restriction of intramolecular motions (RIM) and are an important mechanism to which the AIE phenomena are ascribed.<sup>3, 8, 9</sup>

Previous work in our group focused on the effect of  $\pi$ heterocyclic units in an isoindigo-based donor-acceptor-donor  $(D-\pi-A-\pi-D)$  small molecule fluorophore to afford a series of four fluorophores where triphenylamine (TPA) was employed as an auxiliary donor unit.7 The 3,4-ethylenedioxythiophene (EDOT) derivative, II-EDOT-TPA, exhibited notable theoretical and experimental results suggesting AIE behavior. The HOMO was primarily localized on the EDOT-TPA donor unit, while the LUMO was found to be localized on the isoindigo acceptor indicative of intramolecular charge transfer (ICT). Relative to the other  $\pi$ -heterocyclic units in the series, the EDOT moiety provided an enhanced electron-donating strength as a result of the ether moiety, which decreases the HOMO-LUMO energy gap. 11 The II-EDOT-TPA fluorophore possessed absorption (  $\lambda_{max}^{abs}$ ) and emission ( $\lambda_{max}^{emi}$ ) peak maxima of 640 nm and 805 nm, respectively, with a large Stokes shift of 165 nm (0.39 eV). However, photophysical studies in solution phase revealed low quantum yield (<1%) and short excited-state lifetime (<200 ps) values. Interestingly, a comparison of the predicted ground (S<sub>0</sub>) and excited (S<sub>1</sub>) state geometries for **II-EDOT-TPA** revealed the underlining cause for these experimental findings. Upon excitation, the bond angle between the two aromatic indole units becomes distorted ( $S_0=14.26^{\circ}$  to  $S_1=28.27^{\circ}$ ) (Figure 1). Upon relaxation from the excited state to the ground state, a large amount of energy is required to reorganize and is subsequently lost to non-radiative pathways. 12 This detracts from the energy emitted as radiation and is an important contributor to the low quantum yield and excited-state lifetime values.13, 14

Using the results from our previous work as well as those of others, <sup>15, 16</sup> we aimed to study **II-EDOT-TPA** and its AIE properties in varied environments. In this work, we sought to restrict the change in bond angle between the two aromatic indole units, according to the RIM mechanism, and harness the potential AIE properties of the fluorophore. Herein, we studied **II-EDOT-TPA** and its AIE properties as both the fluorophore encapsulated in a polymer nanoparticle and as a self-assembling amphiphile. **II-EDOT-TPA** was first studied in the solid-state and then in a THF:H<sub>2</sub>O mixture. It was then encapsulated into an amphiphilic linear dendritic block copolymer (LDBC). The optical properties of the resulting nanoaggregates (NAs) were studied, and minimal cytotoxicity was observed. In parallel, the PEGylated derivative of **II-EDOT-TPA** (**PEG-II-EDOT-TPA**) was synthesized and found to form

spherical aggregates upon introduction to aqueous media The photophysical properties of both were studied in addition to their ability to act as potential NIR bioimaging agents.

#### **Experimental**

#### **Materials and Methods**

All materials and reagents were purchased from Sigma-Aldrich (St. Louis, MO, USA) and were used without further modification unless noted otherwise. All the synthetic procedures were conducted under an ultra-purified nitrogen atmosphere using standard Schlenk line techniques unless otherwise stated. Anhydrous solvents were obtained from a Glass Contour solvent purification system (Irvine, CA, USA). Thin-layer chromatography (TLC) was performed using SiO<sub>2</sub>-60 F254 aluminum-backed plates with visualization by ultraviolet (UV) light, while flash column chromatography was performed using a Purasil SiO<sub>2</sub>-60, 230-400 mesh from Whatman. II-EDOT-TPA was synthesized according to the previously published methods.<sup>7</sup> Additional details regarding the synthesis of PEG-II-EDOT-TPA can be found in the ESI.

#### Nanoaggregation

Nanoaggregates for LDBC encapsulated **II-EDOT-TPA** and **PEG-II-EDOT-TPA** were prepared according to the previously reported procedure (ESI).<sup>17,</sup> <sup>18</sup> Particle size and the polydispersity index (PDI) measurements were carried out on a Malvern Instrument Zetasizer Nano ZS using a He—Ne laser with a 633 nm wavelength, a detector angle of 173° at 25° C.

Cryo-TEM was used for **PEG-II-EDOT-TPA** nanoaggregates since PEG possesses a low  $T_g$  value with which cryo-freezing is required in order to maintain the micellar structure that occurs in aqueous solution. For cryo-TEM, grid freezing was carried out using a FEI Mark IV Vitrobot (FEI Co., Hillsboro, OH). Blotting parameters were optimized for each sample; usually two, 1 second blots with a force of 0, +1 or +2 or alternately one, 2 second blot with a force of 0 or -3. Grids were maintained in liquid nitrogen until transferred to a Gatan 626 Single Tilt cryo transfer holder (Gatan Inc., Pleasanton, CA). Grids were imaged in a JEOL 1230 TEM, using 100 kV accelerating voltage. Images were acquired with a Gatan 831 Orius CCD camera and Digital Micrograph software.

Standard TEM was used for the LDBC encapsulated **II-EDOTTPA**. For standard TEM, carbon-coated, 300 mesh grids were plasma cleaned before applying the sample. Negative staining was performed immediately before applying 1% uranyl formate solution to the grid. Grids were imaged by a JEOL 1230 TEM, with a 100 kV accelerating voltage.

#### **Optical and Photophysical Studies**

Solution phase absorption measurements were performed on a Varian Cary-500 spectrometer (Dorval, QC, Canada) in DCM, THF, MeCN, DMSO, and deionized H<sub>2</sub>O at 6.0x10<sup>-4</sup> M concentrations. Solid-state absorption of **II-EDOT-TPA** was performed via diffuse reflectance inside an integrating sphere (ThorLabs Model IS200-4). Concentration studies were

Journal Name ARTICLE

performed in CHCl<sub>3</sub>, which showed comparable solvation of the **PEG** chain, but increased photostability of **PEG-II-EDOT-TPA** when compared to THF. Relative fluorescence quantum ( $\Phi_F$ ) yields were measured using oxazine 750 chloride as a reference due to the relatively low emission from the samples, preventing the use of an integrating sphere. The absolute quantum yield of oxazine 750 chloride was determined to be 11.7%. The  $\Phi_F$  of the samples were calculated using the following equation:

$$\Phi_{F} = \Phi_{F(r)} \left( \frac{A_r}{A_s} \right) \left( \frac{E_s}{E_r} \right) \left( \frac{n_s}{n_r} \right)^2 \tag{1}$$

(where subscripts r and s refer to reference and sample; A = absorption at  $(\lambda_{ex})$ , E = integrated fluorescence intensity, and n = refractive index of the solvent. Excitation for all samples, including the standard, was held at 640 nm.

Femtosecond transient absorption spectroscopy (fsTAS) was used to obtain the excited-state lifetimes for PEG-II-EDOTin organic solvents and the PEG-II-EDOT-TPA nanoaggregates. Optical pulses of sub-100 fs bandwidth were generated using a Ti:sapphire regenerative amplified laser system (Coherent Astrella). The 800 nm fundamental output from the fs amplifier was tuned to the excitation wavelengths used for data acquisition inside an optical parametric amplifier (Light Conversion) before being routed into a transient absorption spectrometer (Ultrafast Systems Helios). Broadband probe pulses for measuring the transient absorption were generated inside the spectrometer by routing a portion of the 800 nm fs pulses through a CaF<sub>2</sub> crystal. Generating the probe pulses in this manner preserves the temporal characteristics of the fundamental pulses for time-resolved measurements and the detection of short lived-transient species. Emission spectra taken using a Horiba Quantamaster were spectrofluorometer with dual excitation gratings and a photomultiplier tube detector for all samples in solution, while solid-state II-EDOT-TPA was analyzed using a Princeton Instruments Acton CCD coupled with a spectrograph and excited using a 650 nm diode laser.

#### In Vitro Cell Uptake and Cytotoxicity Assay

HEK-293 cells were grown under standard conditions (37° C and 5% CO $_2$ ) in DMEM media with 10% FBS. For image particle distribution, HEK-293 cells were exposed to 25  $\mu g/mL$  of particles for one hour. After replacing the cell media, lysosomes were labeled with the lysotracker® Green kit. A Leica SP8 confocal microscope was used to acquire a single optical section of live-cell fluorescence. Cytotoxicity associated with particles was determined by LDH assay. Cells were exposed to a range of particle concentrations for 24 hours followed by colorimetric quantification of LDH enzymes released by damaged cells.

#### Results

Published on 27 April 2022. Downloaded on 4/27/2022 11:34:58 PM

**Optical Characterization of Solid-State II-EDOT-TPA** 

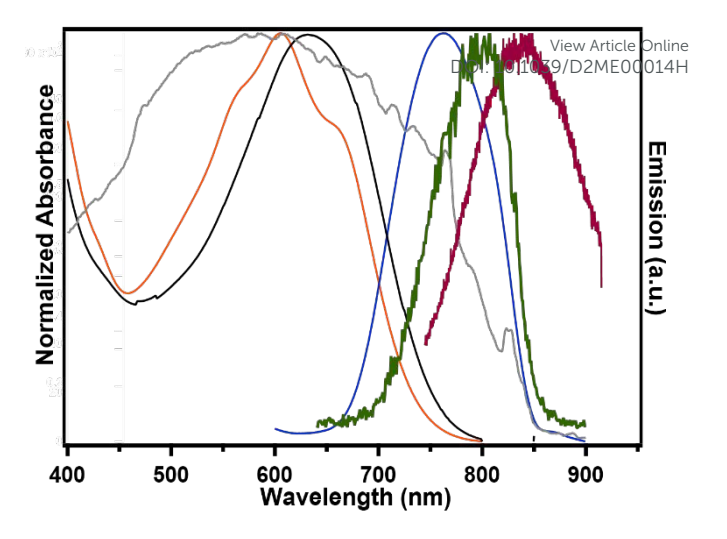


Figure 2. Vis-NIR absorption/fluorescence of LDBC encapsulated II-EDOT-TPA (orange and blue traces) and solid-state II-EDOT-TPA (grey and purple traces) and II-EDOT-TPA in 6x10<sup>-5</sup> M CHCl<sub>3</sub> (black and green traces)

In order to fully understand the photophysical properties of II-EDOT-TPA, we began our work by analyzing II-EDOT-TPA in the solid-state to evaluate its AIE potential. The optical profiles for II-EDOT-TPA are shown in Figure 2. Though broad, the absorption maximum for the amorphous solid-state (AS) of II-EDOT-TPA is positioned at 613 nm with an intensity that is 4.2% less than the previously reported solution state (640 nm, 6 x 10<sup>-5</sup> M in DCM). However, the emission maximum was measured to be 847 nm, with an emission intensity 5.2% greater than that of the solution state (805 nm). Moreover, the excited state lifetime of the  ${\it II-EDOT-TPA}$  in the AS was 399 ps, which is higher than the instrument response function of 200 ps. The solution state lifetime was determined to be less than 200 ps. The increase in AS excited state lifetime along with the increase in emission intensity is indirect evidence that radiative processes are enhanced as aggregation is increased. Comparatively, this data illustrates the enhancement of the optical properties for II-EDOT-TPA in solid-state.

When comparing II-EDOT-TPA in solution versus the solidstate (Fig. 2; ESI Fig. S6), solid-state II-EDOT-TPA is seen to possess a distinct optical profile. The full width at half maxima (FWHM) of absorption spectra gradually broadens from 150 nm in solution to 300 nm in the solid-state and its  $\lambda_{max}^{abs}$  appears blue-shifted by 27 nm. The broadening is indicative of differing molecular arrangements in the solid-state. Upon excitation at 613 nm, a narrow emission band is obtained at 847 nm. With these results, we hypothesize the presence of both H- and Jtype aggregates in the solid-state<sup>20</sup> where the J-aggregates are most likely giving rise to the emission profile. It is known that Htype aggregation can quench fluorescence, so the appearance of a red-shifted emission peak is indicative of the presence of Jtype aggregates. While the presence of H- and J- aggregates cannot be confirmed directly, our data indicate the possibility of both aggregation motifs being present. Alternatively, the observed shifts in the optical properties can also be a result of molecular conformation changes in the aggregate or solidstate.21

Published on 27 April 2022. Downloaded on 4/27/2022 11:34:58 PM

ARTICLE Journal Name

The excited-state lifetime of solid-state **II-EDOT-TPA** (399 ps) is longer when compared to **II-EDOT-TPA** in solution (<200 ps). This increase is presumably due to the restriction of intramolecular rotations and a larger intermolecular  $\pi$ - $\pi$  distance, which are indicative of the AIE phenomenon. <sup>22</sup>

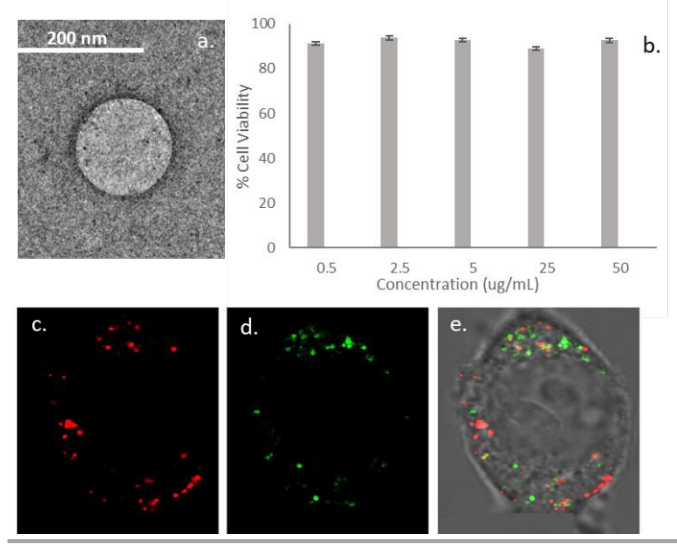


Figure 3. TEM of LDBC encapsulated II-EDOT-TPA nanoparticles (10000x) (a) Percent cell viability of HEK-293 cells incubated with LDBC encapsulated II-EDOT-TPA at varying concentrations (b), HEK-293 cells incubated with LDBC encapsulated II-EDOT-TPA (c), Lysotracker green (d), and merged (e)

Unfortunately, we were not able to obtain quantum yields for solid-state **II-EDOT-TPA** due to re-absorption of the emitted radiation by the sample. Note that in the solution state (6 x 10<sup>-5</sup> M DCM) unrestricted rotation around the single bonds during the first excited state (S1) to ground state (S0) transition results in energy loss via non-radiative pathways. Due to the dense packing associated with the solid-state, <sup>23</sup> intramolecular rotation is restricted. This results in increased radiative decay of the excited state energy while correspondingly minimizing energy loss via non-radiative decay pathways.

#### **Aggregation Induced Emission and Encapsulation**

To further investigate AIE behavior, a series of solutions were prepared with different ratios of organic solvent (THF) and water. The emission intensities of **II-EDOT-TPA** in each solution were measured. When increasing the water content from 1:3 to 3:1 (H<sub>2</sub>O:THF), a general increase in emission intensity was observed. As **II-EDOT-TPA** is highly hydrophobic, it exhibits extremely poor water solubility. As water forces **II-EDOT-TPA** to change its phase from solution to aggregated state, an increasing emission intensity with the increasing water content is achieved. The most significant increase in emission intensity was observed when **II-EDOT-TPA** was dissolved in a THF: H<sub>2</sub>O (1:2) solution. The observed  $\lambda_{max}^{abs}$  was 626 nm, and the  $\lambda_{max}^{em}$  was 786 nm.; thus, providing further evidence for its AIE properties (ESI Fig. S7).<sup>23</sup>

Based on both the solid-state data and aggregation results, we formulated nanoaggregates of **II-EDOT-TPA** using an amphiphilic linear dendritic block copolymer (LDBC) comprised

of a polyester and polyamide (ESI Fig. S8). <sup>18</sup> Previous work with the LDBC resulted in bi-layered vesicles in added to media. The cationic LDBC design showed enhanced properties than its neutral (-OH) and anionic (COO¹) counterparts. <sup>18</sup> The hydrophobic **II-EDOT-TPA** fluorophore would then be encapsulated into the hydrophobic portion of the vesicle. Dye loading (DL) and encapsulation efficiencies (EE) for the encapsulated **II-EDOT-TPA** were found to be 13.2% and 35%, respectively.

Dynamic light scattering was used to analyze the encapsulated **II-EDOT-TPA** nanoaggregates to determine their size in an aqueous environment (ESI Fig. S17, Table S1). Encapsulated **II-EDOT-TPA** nanoaggregates were found to possess an average hydrodynamic radius of 225.9 nm with a polydispersity index (PDI) of 0.213. TEM provides additional evidence for successful nano-assembly where spherical aggregates of 179.2 nm can be seen (Fig 3). Based on the composition of the LDBC and **II-EDOT-TPA** the resulting nanoaggregate morphology is anticipated to be one in which the hydrophilic polyamide extends towards the water surface, protecting the hydrophobic **II-EDOT-TPA** and polyester within the core.<sup>18</sup>

After encapsulation, the II-EDOT-TPA possessed a dark blue clear solution in water (ESI Fig. S9). The measured  $\lambda_{max}^{abs}$  for the encapsulated **II-EDOT-TPA** in water was 606 nm, and the  $\lambda_{max}^{em}$ was 756 nm. The total excited state lifetime (τ) was evaluated before and after encapsulation. The "free" II-EDOT-TPA in solution decays with a single exponential and a lifetime of 108 ps. Encapsulated II-EDOT-TPA displays a double exponential decay with a fast component of around 87 ps and a slow component at 293 ps (ESI Fig. S10). The fast component can be representative of any "monomeric" molecules in the nanoaggregate, while the slow component is the result of aggregated molecules in the nanoaggregate. Given the dramatically longer lifetime of II-EDOT-TPA in the encapsulated state, the dye-nanoparticle interactions can induce an extended excited-state lifetime. This can be explained by excite-state delocalization processes that occur in the solid-state<sup>24</sup> and/or a result of suppressed non-radiative decay due to the RIM effect in the molecular aggregations.<sup>25</sup> The quantum yield (QY) for free II-EDOT-TPA was less than 1%, while an increase in QY to 2.61% was seen for the encapsulated II-EDOT-TPA.

#### Cellular Uptake of Encapsulated II-EDOT-TPA

HEK-293 cell lines were treated with II-EDOT-TPA nanoaggregates to determine cytotoxicity and assess its potential as a bioimaging agent. Epithelial HEK-293 cells were used due to their rapid proliferation and low maintenance.  $^{26}$  The HEK-293 cell line was also specifically chosen as it would be representative of luminal cells that the nanoparticle systems would encounter in the human body. Despite having a positive surface charge of 30.6 mV, cytotoxicity values were noticeably low across a range of concentrations (0.5  $\mu g/mL$  to 50  $\mu g/mL$ ) with less than 12% cell death observed. Encapsulated II-EDOT-TPA was found to be partially internalized in the lysosomes of the HEK-293 cells, with nanoparticles also being observed in the cytoplasm and unmarked organelles. Complete cytotoxicity

Journal Name ARTICLE

View Article Online DOI: 10.1039/D2ME00014H

Table 1. Photophysical data for II-EDOT-TPA and PEG-II-EDOT-TPA

#### II-EDOT-TPA

Solvent	λ <sup>abs</sup> (nm)	$\lambda_{max}^{em}$ (nm)	Stokes shift nm (eV)	Relative QY Φ <sub>F</sub> (%)	ε (x10³ M <sup>-1</sup> cm <sup>-1</sup> )	Lifetimes (ps)	
DCM	640	805	165 (0.40)	0.017	4.3	τ <sub>1</sub> = 108	
Solid-state	613	847	233 (0.55)			τ <sub>1</sub> = 399*	
LDBC NP	606	756	150 (0.40)	2.61	150.0	τ <sub>1</sub> = 87	τ <sub>2</sub> = 293

#### PEG-II-EDOT-TPA

Solvent	λ <sup>abs</sup> (nm)	$\lambda_{max}^{em}$ (nm)	Stokes shift nm (eV)	Relative QY Φ <sub>F</sub> (%)	ε (x10³ M <sup>-1</sup> cm <sup>-1</sup> )	Lifetimes (ps)	
DCM	597	683,741	144 (0.40)	0.25	11.0	τ <sub>1</sub> = 13	τ <sub>2</sub> = 42
THF	600	756	156 (0.42)	3.52	6.56	τ <sub>1</sub> = 10	τ <sub>2</sub> = 65
MeCN	591	685,755	164 (0.45)	0.30	12.5	τ <sub>1</sub> = 5	τ <sub>2</sub> = 13
DMSO	602	770	168 (0.44)	0.40	12.4	τ <sub>1</sub> = 12	
PEG NP	624	815	191 (0.46)	0.22	14.7	τ <sub>1</sub> = 10	τ <sub>2</sub> = 57

<sup>\*</sup>Reported lifetime value for solid-state **II-EDOT-TPA** corresponds to the photoluminescent lifetime rather than total excited state lifetime as obtained from TAS measurements; NP - nanoparticle.

data and confocal fluorescence images of the HEK-293 cells incubated with encapsulated **II-EDOT-TPA** are found in Figure 3.

# PEG-II-EDOT-TPA in Organic Solvents

Published on 27 April 2022. Downloaded on 4/27/2022 11:34:58 PM

An alternative to the encapsulated **II-EDOT-TPA** is the formation of a self-assembling amphiphile of **II-EDOT-TPA**, **PEG-II-EDOT-TPA**. The synthesis of **PEG-II-EDOT-TPA** allows us to avoid some of the drawbacks of the encapsulation strategy, such as poor loading efficiencies and destabilization of the resulting nanoaggregate.<sup>27</sup>

For this aspect of the study, we take advantage of the nitrogens on the isoindigo core to create a polyethylene glycol (PEG) derivative in lieu of the alkyl chains. PEG is a well-studied biocompatible polymer that has been used in numerous applications due to its low cytotoxicity in vivo and its ability to increase solubility in polar/aqueous environments.<sup>28, 29</sup>

Although the PEG chains do not contribute to the  $\pi$ -orbital overlap in **II-EDOT-TPA**, it can affect the photophysical properties of the dye due to its chain length and physicochemical properties of the polymer. Fluorescence properties are highly sensitive to environmental effects. <sup>30</sup> In this case, we expect the polymer-dye (i.e., PEG to **II-EDOT-TPA**) interactions to vary depending on the solvation of the PEG chain. Polymers, like that of PEG, are known to form microenvironments. With varying solvent polarity, the difference in chemical properties between PEG and **II-EDOT-**

**TPA** can induce a difference in the molecular arrangement as well as shielding of the **II-EDOT-TPA** backbone—all of which will give rise to unique photophysical outcomes.

We first investigated **PEG-II-EDOT-TPA** in various organic solvents (Figs. 4, 5 and Table 1). A small bathochromic shift is seen in the absorption peak maxima (Fig. 4) when the solvent changes from DCM ( $\lambda_{max}^{abs}$  = 597 nm) to DMSO ( $\lambda_{max}^{abs}$  = 602 nm). Interestingly, the emission profiles of **PEG-II-EDOT-TPA** in various organic solvents show a striking dependence on solvent polarity. The normalized emission profiles can be seen in Figure 5. As the solvent changes from THF to DMSO to DCM, a higher energy emission peak becomes more prominent while the intensity of the lower energy peak remains essentially constant. When dissolved in MeCN, a hypochromic shift of the lower energy peak is seen, while a hyperchromic shift of the higher energy peak occurs.

To justify this trend, we account for solvation-dependent aggregation that is due to PEG-solvent interactions. The large PEG chain can interact with both solvent molecules and the  $\pi$ -framework of the **II-EDOT-TPA**. Therefore, various aggregates can be present due to a solvation balance between the three: solvent molecules, PEG, and **II-EDOT-TPA**. It has been reported that PEG shows a decrease in solubility when changing solvents from THF to DMSO to MeCN. $^{31}$  THF and DMSO are generally considered good solvents for PEG, while MeCN has been shown to display moderate solvating abilities. Here, solvation is an important factor in influencing the micro-environment surrounding the fluorophore induced by the PEG chains. In

Published on 27 April 2022. Downloaded on 4/27/2022 11:34:58 PM

ARTICLE Journal Name

MeCN, the predominant emissive peak at 685 nm is indicative of high energy aggregates. **PEG-II-EDOT-TPA** in DCM yields an emission spectrum that exhibits a similar peak at 683 nm

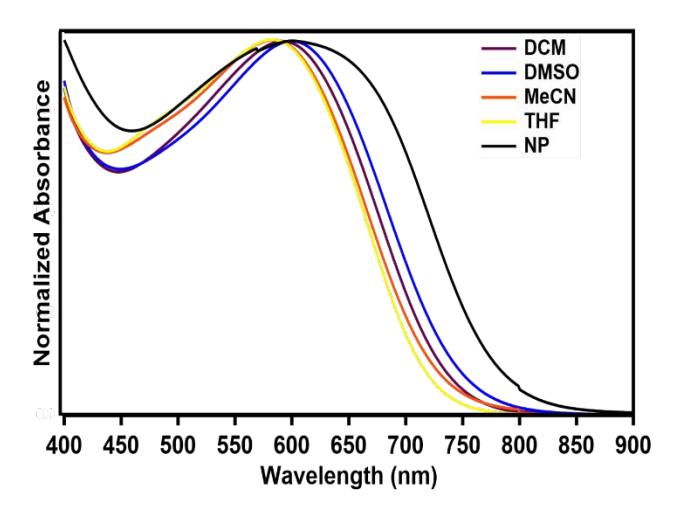


Figure 4. Vis-NIR absorption of PEG-II-EDOT-TPA in organic solvents ( $6.0x10^4$  M) and 1 mg/mL solution of PEG-II-EDOT-TPA in water as a nanoparticle.

alongside a more pronounced emissive peak at 760 nm suggesting comparable amounts of the high energy aggregates and an emissive lower energy aggregate characterized as an excimer.<sup>32</sup> In DMSO and THF, the predominant lower energy emission peak is evident, indicating a greater abundance of the excimer formations.<sup>33</sup> The complete photophysical data can be found in Table 1.

The abovementioned results indicate the presence of multiple emissive aggregate assemblies whose spectral signatures vary depending on the solvent. To better understand PEG-II-EDOT-TPA in organic solvent, we performed a concentration-dependent study in CHCl<sub>3.</sub>31 Using a solvent in which the PEG chains and  $\pi$ -framework of the **II-EDOT-TPA** are fully solubilized at low concentration aids in correlating the photophysical trends observed to the type of aggregate being present in solution. PEG-II-EDOT-TPA at 7.0x10-4 M CHCl<sub>3</sub> affords  $\lambda_{max}^{em}$  790 nm. However, as the concentration is decreased, there is a hypsochromic shift observed along with the appearance of a higher energy shoulder peak that gradually increases in intensity. From these results, we can conclude that the high energy peaks correspond to a more "monomer-like" emissive species while those at low energy are highly structured aggregates. Interestingly, we observed little to no changes in the absorption spectra, suggesting that these aggregates are present at low concentrations.<sup>33</sup> Nonetheless, it is clear that the PEG-solvent interactions induce multiple molecular arrangements, which give rise to unique emissive signatures (ESI Fig. S11).

#### Transient Absorption Spectroscopy (TAS)

TAS was performed to measure excited state lifetime values and further solidify our solvation-induced aggregation hypothesis. When compared to both LDBC encapsulated **II-EDOT-TPA** (87

ps and 293 ps) and solution-state II-EDOT-TPA (108 ps) the lifetime measurements were much lower Base of the lifetime base of the lifetime measurements were much lower base of the lifetime base of the lifet profiles (Figure 5), we expected the lifetime values for PEG-II-EDOT-TPA in DMSO to be like those seen in THF and DCM (i.e., longer lifetime values), while that of PEG-II-EDOT-TPA in MeCN would be much shorter. This hypothesis is based on the emission spectra in Figure 5, indicating similar aggregation forms for PEG-II-EDOT-TPA in DMSO, THF, and DCM with PEG-II-EDOT-TPA in MeCN having a different aggregation form, as previously stated. Surprisingly, however, lifetime measurements seem to correlate more with trends in dielectric constant for the solvent rather than aggregation behavior. TAS showed that the transient species show a red-shift in the absorption maxima in MeCN and DMSO ( $\lambda_{max}^{abs}$ = 505 and 750 nm) when compared to the transient species in THF ( $\lambda_{max}^{abs}$  = 450 and 720 nm). This difference indicates that the species in THF is potentially in a lower energy conformation relative to the transient species in MeCN and DMSO. The decay curve of PEG-II-EDOT-TPA in THF exhibits a bi-exponential character with the first component (10 ps) being comparable to what is observed in DMSO and MeCN (12 and 5.5 ps, respectively) (ESI Fig. S15-S20). The variation in lifetime measurements is likely attributed to the difference in the dielectric constant. The longer-lived excited state species are a result of the lower dielectric constant values for THF (7.58 F/m) and DCM (8.93 F/m). DMSO and MeCN have higher dielectric constants, 46.7 and 37.5 F/m, respectively, which accounts for the much shorter excited state lifetime values.34 Full TAS spectra can be found in the ESI Fig. S12-S16.

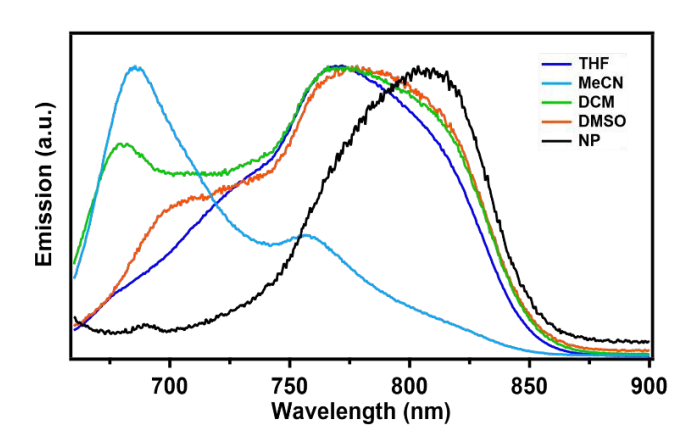


Figure 5. PEG-II-EDOT-TPA fluorescence in organic solvents ( $6.0x10^{-4}$  M) and PEG-II-EDOT-TPA nanoaggregates (1 mg/mL solution)

#### PEG-II-EDOT-TPA in Aqueous Media

**PEG-II-EDOT-TPA** formed nanoaggregates through nanoprecipitation methods. With this nano-assembly, we hypothesized that **PEG-II-EDOT-TPA** would form micellar nanoaggregates in aqueous media. In this case, the hydrophilic PEG chains would act as the corona surrounding the hydrophobic fluorophore to create spherical **PEG-II-EDOT-TPA** nanoaggregates. The resulting nanostructures were studied via DLS (ESI Fig. S18, Table S1) and TEM (Figure 6a). The average

Journal Name ARTICLE

hydrodynamic radius was found to be 124.3 nm with an average PDI of 0.253. Analysis by TEM **PEG-II-EDOT-TPA** nanoaggregates provided sizes larger than 200 nm where secondary aggregation appears to dominate. The  $\lambda_{max}^{abs}$  and  $\lambda_{max}^{em}$  for **PEG-II-EDOT-TPA** nanoaggregates were found to be 624 nm and 815 nm, respectively. Excited-state lifetimes of **PEG-II-EDOT-TPA** nanoaggregates were bi-exponential with values of 9.60 and 50.7 ps. Although the nanoaggregate sizes and absorption maxima are similar, the emission maxima and lifetime for **PEG-II-EDOT-TPA** and encapsulated **II-EDOT-TPA** in water are dramatically different, presumably due to the difference in aggregation behavior of the  $\pi$ -framework.

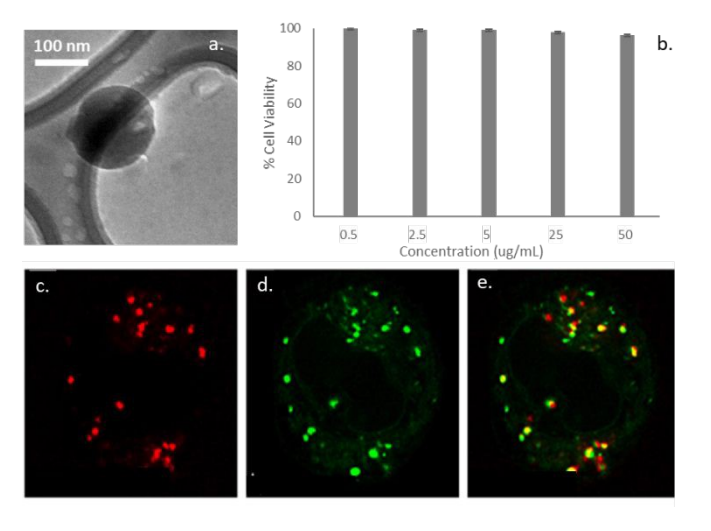


**Figure 6.** TEM of **PEG-II-EDOT-TPA** nanoaggregates at a magnification of 10000x (a) Percent cell viability of HEK-293 cells incubated with **PEG-II-EDOT-TPA** nanoaggregates at varying concentrations (b) HEK-293 cells incubated with **PEG-II-EDOT-TPA** nanoaggregates (c), Lysotracker green (d), and merged (e)

#### Cellular Uptake of PEG-II-EDOT-TPA NPs

Human embryonic kidney (HEK-293) cells were utilized for cellular imaging and cytotoxicity studies. Cytotoxicity was measured using the LDH assay method after incubation with a range of nanoaggregate concentrations per mL of cell culture medium. Significant cell death (<20%) was only observed at a concentration of 150  $\mu g/mL$ . The **PEG-II-EDOT-TPA** nanoaggregates were found to accumulate in the lysosomes of the HEK-293 cells, as evident when overlapped with the HEK-293 cells incubated with Lysotracker Green (Figure 6c-e). Such accumulation is expected as the **PEG-II-EDOT-TPA** nanoaggregates do not have any functionality on the hydrophilic portion rendering a nanoaggregate with a neutral surface.

# Discussion

Published on 27 April 2022. Downloaded on 4/27/2022 11:34:58 PM

For this study, we compared the optical and photophysical properties of **II-EDOT-TPA** in solution and solid-state to that of its encapsulated and amphiphilic forms. Each aspect of the study provided insight on the ability of **II-EDOT-TPA** to act as an

AlE dye for potential in bioimaging applications. The absorption peak maxima of the solid-state **II-EDOT-TPA** Is 1870 and slightly blue-shift when compared to **II-EDOT-TPA** in solution. The solid-state **II-EDOT-TPA** spectrum indicates the presence of both H-and J-type aggregates. The emission spectra of solid-state **II-EDOT-TPA** supports this observation, where a narrow red-shifted peak at 844 nm is seen. This is, of course, common for solid-state studies in which the propensity to form various aggregates via  $\pi$ -  $\pi$  stacking results in differing emissive states.  $^{20}$ 

Encapsulated II-EDOT-TPA possesses an absorption spectrum with more well-defined spectral features and an  $\lambda_{max}^{abax}$  that is hypsochromically shifted when compared to II-EDOT-TPA in solution and solid-state. The noticeable higher and lower energy shoulder peaks seen in the absorption spectra for the encapsulated II-EDOT-TPA are presumably due to vibronic transitions. We did observe an increase in emission intensity as noted due to the increase of fluorescence quantum yield confirming AIE properties.

Interestingly, the modified version of the fluorophore, **PEG-II-EDOT-TPA** shows the ability to form solvent-dependent aggregates that give rise to unique emissive species. These properties were attributed to excimer formation and not AIE.<sup>33</sup>, The type of aggregate formed is heavily dependent on the solvent being used as different micro-environments are induced by the PEG chains. **PEG-II-EDOT-TPA** in THF shows primarily one broad emission peak, but when changing from DMSO to DCM, a higher shoulder peak becomes more prevalent. In MeCN, the higher energy peak is most prominent, while the lower energy emissive peak is reduced in intensity.

Fortunately, nanoaggregates of **PEG-II-EDOT-TPA** displayed further red-shifting in both the absorption and emission spectra. We did observe a slight increase in relative quantum yield for the **PEG-II-EDOT-TPA** nanoaggregates (0.22%), but it was not on par with the increase seen for the LDBC encapsulated **II-EDOT-TPA** nanoaggregates (2.6%). The differing photophysical properties of the two nanoaggregates are owed to differences in intermolecular interactions occurring within the nanoaggregates. For the **PEG-II-EDOT-TPA** nanoaggregates, the photophysical properties are attributed to the presence of excimeric species within the nanoaggregate. However, the photophysical properties for the LDBC encapsulated **II-EDOT-TPA** nanoaggregates are the result of intermolecular interactions that result in the AIE properties seen.

Encapsulated II-EDOT-TPA and the PEG-II-EDOT-TPA nanoaggregates were also subjected to cellular uptake and cytotoxicity studies. The encapsulated II-EDOT-TPA and PEG-II-EDOT-TPA nanoaggregates exhibited minimal cytotoxicity (<20%). Both nanoaggregate solutions were found internalized in the lysosomes of the HEK-293 cells, while the encapsulated II-EDOT-TPA was also found in other cell organelles as there was no overlap of the organelles with the Lysotracker green agent. The hydrophilic portion of the LDBC encapsulated II-EDOT-TPA consists of cationic functionalities, which assist in cellular uptake, while the hydrophilic portion of the PEG-II-EDOT-TPA nanoaggregate is comprised of methoxy functional groups. Neither nanoaggregate system should be affected by the pH of

ARTICLE Journal Name

the lysosome as the LDBC system is already protonated while the methoxy terminated PEG system will not be protonated in the lysosomal media. Interestingly, a comparison of the confocal fluorescence cell images shows that the PEG-II-EDOT-TPA nanoaggregates appear more efficient regarding cellular uptake. This can be correlated to the size of the PEG-II-EDOT-TPA nanoparticles as they are larger than the LDBC encapsulated II-EDOT-TPA nanoparticles. The PEG-II-EDOT-TPA nanoparticles do not move as freely in the cell media as the smaller encapsulated II-EDOT-TPA nanoparticles. Such observations suggest an additional advantage of further utilizing the self-assembling amphiphile as a bioimaging agent.

#### **Conclusions**

Published on 27 April 2022. Downloaded on 4/27/2022 11:34:58 PM

The two encapsulation approaches studied in this work illustrate how photophysical properties can be affected by aggregation behavior. Encapsulation into a LDBC led to the formation of nanoaggregates with which the AIE properties of the isoindigo fluorophore were exploited, displaying an increase in  $\Phi_{\text{F}}$  relative to that of the free fluorophore in solution. Replacement of the alkyl chains with PEG created an amphiphilic version of the isoindigo fluorophore. Micellar-like nanoaggregates were obtained upon nanoprecipitation where a notable red-shift in emission due to excimeric-type aggregation within the nanoaggregate was observed. Both nanoaggregate forms possessed minimal cytotoxicity and exhibited promising properties as bioimaging agents.

As we progress this work, crystallographic data and further computational work would be needed to corroborate our results and correlate them to more recently proposed AIE mechanisms.<sup>6, 8, 9</sup> Nonetheless, we will use the results of this work to design NIR-emissive fluorophores and employ both methods used to exploit the different properties in order to make more efficient FI agents.

#### **Author Contributions**

<sup>‡</sup> Equal intellectual contribution

#### **Conflicts of interest**

There are no conflicts to declare.

### **Acknowledgements**

The authors would like to thank Mississippi INBRE (P20GM103476) and National Science Foundation (CBET MRI 2019023 and OIA 1757220) for providing the funding for this study.

## **Notes and references**

 J. Mei, N. L. C. Leung, R. T. K. Kwok, J. W. Y. Lam and B. Z. Tang, Chem. Rev., 2015, 115, 11718-11940.

- Y. Li, S. Liu, H. Ni, H. Zhang, H. Zhang, C. Chuah, C. Ma Kinse Wong, J. W. Y. Lam, R. T. K. Kwokodi: @iaŋ:※/此函和他跟4程 Tang, *Angew. Chem. Int. Ed.*, 2020, **59**, 12822-12826.
- Y. Chen, J. W. Y. Lam, R. T. K. Kwok, B. Liu and B. Z. Tang, Mater. Horiz., 2019, 6, 428-433.
- S. G. R, M. Pandey and A. S. J. Chakravarthy, *Mater. Chem. Front.*, 2021, **5**, 1541-1584.
- J. Luo, Z. Xie, J. W. Y. Lam, L. Cheng, H. Chen, C. Qiu, H. S. Kwok, X. Zhan, Y. Liu, D. Zhu and B. Z. Tang, Chem. Commun., 2001, DOI: 10.1039/B105159H, 1740-1741.
- Z. Zhao and B. Z. Tang, Natl. Sci. Rev., 2021, 8.
- S. M. Vijayan, N. Sparks, J. K. Roy, C. Smith, C. Tate, N. I. Hammer, J. Leszczynski and D. L. Watkins, *J. Phys. Chem. A*, 2020, 124, 10777-10786.
- 8. Q. Peng and Z. Shuai, *Aggregate*, 2021, **2**, e91.
- 9. J. Yang, M. Fang and Z. Li, Aggregate, 2020, 1, 6-18.
- D. Ding, K. Li, B. Liu and B. Z. Tang, Acc. Chem. Res., 2013, 46, 2441-2453.
- S. Ellinger, K. R. Graham, P. Shi, R. T. Farley, T. T. Steckler, R. N. Brookins, P. Taranekar, J. Mei, L. A. Padilha, T. R. Ensley, H. Hu, S. Webster, D. J. Hagan, E. W. Van Stryland, K. S. Schanze and J. R. Reynolds, *Chem. Mater.*, 2011, 23, 3805-3817.
- S. Goswami, M. K. Gish, J. Wang, R. W. Winkel, J. M. Papanikolas and K. S. Schanze, ACS Appl. Mater. Interfaces, 2015, 7, 26828-26838.
- 13. P. Horváth, P. Šebej, T. Šolomek and P. Klán, *J. Org. Chem.*, 2015, **80**, 1299-1311.
- Z. Zhang, G. Zhang, J. Wang, S. Sun and Z. Zhang, *Comput. Theor. Chem.*, 2016, 1095, 44-53.
- 15. W. Xu, D. Wang and B. Z. Tang, *Angew. Chem. Int. Ed.*, 2021, **60**, 7476-7487.
- M. Kang, Z. Zhang, N. Song, M. Li, P. Sun, X. Chen, D. Wang and B. Z. Tang, *Aggregate*, 2020, 1, 80-106.
- Y. Wu, K. Wang, S. Huang, C. Yang and M. Wang, ACS Appl. Mater. Interfaces, 2017, 9, 13602-13610.
- I. Chandrasiri, D. G. Abebe, M. Loku Yaddehige, J. S. D. Williams, M. F. Zia, A. Dorris, A. Barker, B. L. Simms, A. Parker, B. P. Vinjamuri, N. Le, J. N. Gayton, M. B. Chougule, N. I. Hammer, A. Flynt, J. H. Delcamp and D. L. Watkins, ACS Appl. Bio Mater., 2020, 3, 5664-5677.
- S. Dawood, A. Dorris, K. Davis, N. I. Hammer and H. Rathnayake, J. Phys. Chem. C., 2021, 125, 792-802.
- M. Kirkus, L. Wang, S. Mothy, D. Beljonne, J. Cornil, R. A. J. Janssen and S. C. J. Meskers, *J. Phys. Chem. A*, 2012, **116**, 7927-7936.
- Y. Ji, Z. Peng, B. Tong, J. Shi, J. Zhi and Y. Dong, *Dyes Pigm.*, 2017, 139, 664-671.
- M. Jiang, Z. He, Y. Zhang, H. H. Y. Sung, J. W. Y. Lam, Q. Peng, Y. Yan, K. S. Wong, I. D. Williams, Y. Zhao and B. Z. Tang, J. Mater. Chem., 2017, 5, 7191-7199.
- Y. Ren, A. K. Hailey, A. M. Hiszpanski and Y.-L. Loo, *Chem. Mater.*, 2014, 26, 6570-6577.
- D. B. Sulas, A. E. London, L. Huang, L. Xu, Z. Wu, T. N. Ng, B.
  M. Wong, C. W. Schlenker, J. D. Azoulay and M. Y. Sfeir, *Adv. Opt. Mater.*, 2018, 6, 1701138.
- S. Suzuki, S. Sasaki, A. S. Sairi, R. Iwai, B. Z. Tang and G.-i. Konishi, *Angew. Chem. Int. Ed.*, 2020, **59**, 9856-9867.
- P. Thomas and T. G. Smart, J. Pharmacol. Toxicol. Methods, 2005, 51, 187-200.
- C. Jeong, I. Noh, N. S. Rejinold, J. Kim, S. Jon and Y.-C. Kim, *ACS Biomater. Sci. Eng*, 2020, 6, 474-484.

View Article Online

DOI: 10.1039/D2ME00014H

**Journal Name ARTICLE** 

- 28. M. Lee and S. W. Kim, Pharm. Res., 2005, 22, 1-10.
- 29. K. Knop, R. Hoogenboom, D. Fischer and U. S. Schubert, Angew. Chem. Int. Ed., 2010, 49, 6288-6308.
- 30. A. Boreham, R. Brodwolf, K. Walker, R. Haag and U. Alexiev, Molecules, 2017, 22, 17.
- 31. C. Özdemir and A. Güner, Eur. Polym. J., 2007, 43, 3068-3093.
- 32. R. T. Grant, P. Michetti, A. J. Musser, P. Gregoire, T. Virgili, E. Vella, M. Cavazzini, K. Georgiou, F. Galeotti, C. Clark, J. Clark, C. Silva and D. G. Lidzey, Adv. Opt. Mater., 2016, 4, 1615-1623.
- 33. A. J. Musser, S. K. Rajendran, K. Georgiou, L. Gai, R. T. Grant, Z. Shen, M. Cavazzini, A. Ruseckas, G. A. Turnbull, I. D. W. Samuel, J. Clark and D. G. Lidzey, J. Mater. Chem., 2017, **5**, 8380-8389.
- 34. S. Babiak and A. C. Testa, J. Phys. Chem., 1974, 78, 201-202.
- 35. H. Shi, X. He, Y. Yuan, K. Wang and D. Liu, Anal. Chem., 2010, 82, 2213-2220.
- 36. Y. Shen, Z. Zhang, H. Liu, Y. Yan, S. Zhang, B. Yang and Y. Ma, J. Phys. Chem. C., 2019, 123, 13047-13056.

Published on 27 April 2022. Downloaded on 4/27/2022 11:34:58 PM.